University of Sistan and Baluchestan

Chemical Process Design

Available online at http://cpd.usb.ac.ir/



Non-Dimensional Benchmarking of Sloshing Simulations in a Pressurized LNG Tank against a Cryogenic Sloshing Correlation

Yahya Balouchi[1], Mortaza Zivdar[2]✉, Rahbar Rahimi[3], Davood Mohebbi-Kalhori[4]

[1] Department of Chemical Engineering, Faculty of Engineering, University of Sistan and Baluchestan, Zahedan, Iran.
E-mail: balouchi.yahya@pgs.usb.ac.ir.
[2] Corresponding Author, Department of Chemical Engineering, Faculty of Engineering, University of Sistan and Baluchestan, Zahedan, Iran.
E-mail: mzivdar@eng.usb.ac.ir
[3] Department of Chemical Engineering, Faculty of Engineering, University of Sistan and Baluchestan, Zahedan, Iran.
E-mail: rahimi@hamoon.usb.ac.ir
[4] Department of Chemical Engineering, Faculty of Engineering, University of Sistan and Baluchestan, Zahedan, Iran.
E-mail: davoodmk@eng.usb.ac.ir

ARTICLE INFO

Article type:

Research Article

Article history:
Received: 2026-09-26
Received in revised form: 2026-10-13
Accepted: 2026-10-18
Available online: 2026-10-18

Keywords: *Pressurized LNG; Sloshing; Interfacial mass transfer; Sloshing Nusselt number; Volume of fluid*

ABSTRACT

Sloshing simulations of cryogenic tanks are usually validated against a single pressure history, which cannot show whether interfacial heat and mass transfer is correct in magnitude or correctly partitioned between quiescent and sloshing-induced contributions. This study benchmarks volume-of-fluid simulations with a Hertz–Knudsen–Schrage closure of a Type-C tank holding a pseudo-pure pressurized LNG mixture ($CH_4/C_2H_6/C_3H_8/N_2$ = 90/6/3/1 mol%, 10–30 bar; CO_2 carried only as a passive tracer) against the sloshing Nusselt–Reynolds correlation of Ludwig et al., using 14 sloshing runs and four matched static runs at a single excitation (0.4 Hz, 3°; Re_S = 1.8–2.2 × 10^5). (1) The extracted sloshing Nusselt numbers (25–66) lie a factor of 1.6–4.8 above the correlation; since the absolute level depends on the effective closure coefficient, this indicates order-of-magnitude consistency only. (2) The static runs give Nu_S = 10.4–18.6 against unity in the unexcited experiment; this cannot be attributed to the closure coefficient and is traced mainly to eddy diffusion of the k–ε model in the stratified static layer. (3) The paired enhancement factor is 2.52–2.69 for a 60 s window (1.3–4.3 depending on the window), about six times below the experimental value. (4) The arrest of boundary-layer growth under sloshing is reproduced qualitatively. Because only one excitation was used, the slope of the correlation is not tested, and the 25 and 30 bar results are qualitative owing to the ideal-gas vapor density.

Cite this article: Balouchi, Y., Zivdar, M., Rahimi, R., Mohebbi-Kalhori, D., (2027), Non-Dimensional Benchmarking of Sloshing Simulations in a Pressurized LNG Tank against a Cryogenic Sloshing Correlation, *Chemical Process Design*, 6(1), 1-14. http//doi.org/10.22111/cpd.2026.57271.1103

© The Author(s).
Publisher: University of Sistan and Baluchestan.
DOI: http//doi.org/10.22111/cpd.2026.57271.1103

ARTICLE IN PRESS

1. Introduction

Pressurized liquefied natural gas (PLNG) is stored at 10–40 bar and at temperatures well above those of conventional LNG, which allows part of the CO_2 in the feed gas to remain dissolved in the cargo. At sea, ship motion makes the liquid slosh. Sloshing continuously renews the liquid–vapor interface and intensifies interfacial heat and mass transfer, so that a tank whose liquid is subcooled with respect to the ullage pressure depressurizes rapidly. This behavior has been documented in cryogenic experiments [1, 2] and in marine LNG fuel tanks [3], and has recently been reviewed [4].

The standard predictive tool is a volume-of-fluid (VOF) simulation [5] combined with an interfacial mass-transfer closure, either temperature-driven, following Lee [6], or pressure-driven, following the Hertz–Knudsen–Schrage (HKS) relation [7]. Both closures carry coefficients that act as effective, cell-scale parameters and are usually tuned or tested against a single experiment [8]. Validation normally rests on one pressure history, often measured with a non-cryogenic fluid near atmospheric pressure [3]. Agreement of a single pressure curve can result from compensating errors, and an independent metric is needed to judge the integral response of a model in a sloshing cryogenic tank.

CFD studies of sloshing in cryogenic and LNG tanks with interfacial phase change are mostly based on VOF interface capturing. Grotle and Æsøy [14] reproduced the mixing-induced pressure drop with a two-dimensional VOF model and the temperature-driven Lee closure and analysed the role of the initial non-equilibrium. Agui and Moder [23] simulated a shaken liquid-nitrogen cryostat in three dimensions with VOF and the Schrage relation in ANSYS Fluent and reported a strong dependence of the depressurization on the accommodation coefficient at low values and on the treatment of turbulence. Wu and Ju [15] showed for a Type-C LNG tank that sloshing can raise the boil-off rate by up to about two orders of magnitude relative to the static tank, and extended the analysis to a wider parametric matrix of fuel tanks [8]. Liu et al. [16] and Liu and Li [17] studied the thermodynamic performance of cryogenic fuel tanks under external excitation and the effect of baffles in a liquid-hydrogen tank; Duan et al. [18] combined numerical and theoretical prediction of the thermodynamic response of marine LNG fuel tanks; Jeon et al. [19, 20] used multiphase-thermal simulation and combined experiment and simulation to estimate boil-off changes due to sloshing; and Zhao et al. [21] and Sun et al. [22] extended the approach to Type-B tanks during emergency stops and to liquid CO_2 in Type-C tanks. These studies are validated mainly against pressure histories or boil-off rates, mostly for single-component fluids. To the authors' knowledge, none of them assesses the magnitude and the partition of the simulated interfacial transfer in dimensionless form against a cryogenic correlation, which is the position of the present work.

Ludwig et al. [2] provided such a metric. Their main contribution is a device-independent correlation between the sloshing Nusselt number, the ratio of an effective diffusivity to the molecular thermal diffusivity of the liquid, and a sloshing Reynolds number built on the realized wave amplitude. The correlation was tested with liquid nitrogen, liquid hydrogen [9] and HFE-7000 [10] over a fifteen-fold range of tank radius. The same study includes an unexcited test, in which the effective diffusivity equals the molecular value, and a reduced-order model of the pressure history. Placing another system on this curve is exactly the use for which the correlation was built.

To the authors' knowledge, a benchmarking of VOF–HKS simulations of a pseudo-pure PLNG mixture, carried out within a CO_2 freeze-out study, against the sloshing Nusselt–Reynolds correlation has not been reported. The cargo is treated as a pseudo-pure fluid and CO_2 is a passive tracer; the benchmark therefore tests the thermo-hydraulic model that underlies the freeze-out assessment, not the transport of CO_2. Three questions are addressed: whether the order

ARTICLE IN PRESS

of magnitude of the simulated interfacial transfer agrees with the experimental data; whether its dependence on thermodynamic state, at a single sloshing intensity, is consistent with the correlation; and whether the mechanism reported experimentally is reproduced. Matched static runs in the simulation matrix permit a fourth question: how the total transfer is partitioned between a static baseline and the sloshing enhancement. The exercise is a non-dimensional benchmarking and not a direct validation; the distinction is set out in Section 2.4.

2. Methods

2.1. Two-phase model and mass-transfer closure

The simulations solve a single set of continuity, momentum and energy equations for the two-phase mixture, and the interface is captured with the VOF method [5] and geometric reconstruction. Interfacial mass transfer follows the HKS relation [7]:

$$\dot{m}'' = \frac{2\sigma}{2-\sigma}\sqrt{\frac{M}{2\pi R}}\left[\frac{p_{sat}(T_l)}{\sqrt{T_l}} - \frac{p_v}{\sqrt{T_v}}\right] \quad (1)$$

where σ is the accommodation coefficient, M the molar mass, R the universal gas constant, T_l and T_v the liquid and vapor temperatures in the cell and p_v the vapor pressure. The surface flux is converted into a volumetric source by multiplying it by an interfacial area density $a_i = [\alpha_l(1-\alpha_l)]^{0.75}/L_{cell}$, whose maximum, $0.354/L_{cell}$, lies about 2.8 times below the value for a sharp interface (the expression is used for $\alpha_l(1-\alpha_l) > 0.01$, linear below, and capped at 500 m^{-1}; it is an implementation choice of the authors and no external source is claimed, and the mass transferred per time step is limited to half of the source-phase mass of the cell). The accommodation coefficient was set to $\sigma = 0.01$, following Agui and Moder [23] and not calibrated for this system. Because a_i scales with the inverse cell size, σ acts here as an effective, cell-scale coefficient rather than a molecular accommodation coefficient, and it should not be transferred to a different mesh or area formulation. Turbulence is modelled with the realizable k–ε model [11] and standard wall functions, without a buoyancy-damping term. The same model is used in the static runs; without buoyancy damping it is known to over-predict eddy diffusion near a free surface (Section 3.3). The solver was validated against the sloshing-induced depressurization measured by Grotle and Æsøy [3]: horizontal cylindrical tank (inner diameter 0.35 m, cylindrical length 0.89 m), water, initial pressure 1.3 bar, 50% fill, ±3° roll at 0.29, 0.40 and 0.57 Hz (f/f_n = 0.43, 0.60 and 0.84), HKS closure with σ = 0.01 and the discretization of the production runs (Supplementary Fig. S1). At 0.40 Hz the mean absolute relative error of the normalized pressure over the first 27 s is 1.3% (RMSE 1.6%, R^2 = 0.98, maximum 2.8%), and the order of the three excitations is reproduced. Beyond about 27 s the simulation over-predicts the pressure drop (9.5% at 40 s), consistent with the accumulation of non-condensable air (initial mass fraction 0.075) in the experimental ullage, which a single-component model cannot represent; the validated window is therefore 0–27 s. The validation is at the hydrodynamic and pressure level (the experimental fluid is water) and does not validate absolute cryogenic interfacial kinetics.

2.2. Geometry, excitation and mesh

The domain is the two-dimensional longitudinal section of an independent Type-C tank, 4 m long and 1.5 m in diameter, following Wu and Ju [8], filled to 50%. Sloshing is imposed as a harmonic roll, $\theta(t) = \theta_A \sin(2\pi f t)$, with θ_A = 3° and f = 0.4 Hz, through rigid-body motion of the mesh. The first-mode natural frequency at this fill is 0.302 Hz, so the frequency ratio is 1.32 and all runs lie away from resonance. The structured mesh has 115,776 cells, the mean equivalent cell size is about 7 mm and falls to about 3.2 mm in the refined band around the interface. Mesh

ARTICLE IN PRESS

independence was assessed with four meshes (38,000–156,000 cells; maximum free-surface height; differences from the production mesh of about 6–9% for the two coarser meshes and about 2% for the finest) and with a grid-convergence index on a √2 triplet (57,888, 115,776 and 231,552 cells) for the normalized pressure and the mean interfacial mass-transfer rate (Supplementary Table S3). On the production mesh the uncertainty bands are about 1.4% for the pressure ratio and 3–6% for the mass-transfer rate, i.e., about 6–12% for D_e and Nu_S through Eq. (8), since D_e scales with the square of the condensed mass. Nu_S and E were not themselves subjected to a convergence study, and because the thermal boundary layer is resolved by fewer than two cells during the first 10 s (Section 3.3), the static baseline in particular may be resolution-sensitive. Each run covers 60 s of physical time, with reports written every 0.25 s. The centre of rotation is the geometric centre of the tank bottom; the solver settings are summarized in Table A1 (Appendix A).

2.3. Thermophysical properties

The cargo is a methane/ethane/propane/nitrogen mixture of molar composition 90/6/3/1, treated as a pseudo-pure fluid. Liquid density, heat capacity, thermal conductivity, viscosity and latent heat were obtained from the GERG-2008 equation of state [12] through CoolProp [13] and fitted as temperature polynomials with errors below 0.2%. Liquid density depends on temperature and no Boussinesq approximation is used, so thermal expansion of the liquid enters the continuity equation directly. Liquid viscosity is built from a cube-root (Kendall–Monroe) mixing rule on the pure components, scaled by 1.325 to match GERG-2008 between 172 and 186 K; its uncertainty below 172 K is estimated at 10–20%.

Vapor density is computed from the ideal-gas law with the effective molar mass of the mixture. Table 1 compares it with GERG-2008 for the equilibrium vapor at the bubble point: the ideal-gas value is 12% low at 10 bar and 30% low at 30 bar. The equilibrium vapor has a molar mass of 17.0 g mol^{-1} at 10 bar and 16.6 g mol^{-1} at 30 bar, so using the mixture value (17.85 g mol^{-1}) overestimates the molar mass and partly offsets the neglect of Z; the tabulated error is the net of two opposing errors. An underestimated vapor density reduces the heat capacity of the ullage and exaggerates the pressure drop. Section 2.5 shows that the Nusselt-number extraction contains no vapor density, whereas the simulated condensed mass and the pressure history do depend on it; the effect on the simulated pressure history is discussed in Section 3.4. The 25 and 30 bar results are therefore regarded as qualitative. Ja and $\rho_{v,s}/\rho_l$ are evaluated with the GERG-2008 saturated-vapor density.

Table 1. Ideal-gas vapor density versus GERG-2008 for the equilibrium vapor of the 90/6/3/1 mixture at the bubble point (ideal gas evaluated with the mixture molar mass, 17.85 g mol^{-1})

p (bar)	T_{bub} (K)	Z	ρ_v, GERG-2008 (kg m^{-3})	ρ_v, ideal gas (kg m^{-3})	Error (%)
10	149.4	0.838	16.35	14.36	−12.2
15	159.5	0.786	24.19	20.18	−16.6
20	167.5	0.739	32.46	25.63	−21.1
25	174.2	0.694	41.34	30.80	−25.5
30	180.1	0.652	51.03	35.75	−29.9

2.4. Simulation matrix and benchmarking approach

The benchmarking uses 18 runs (Table 2): 14 sloshing runs covering 10–30 bar and 4 static runs, each matched to one sloshing run in pressure, CO_2 content and initial state and differing only in the absence of excitation. All runs

ARTICLE IN PRESS

start with the liquid about 10 K subcooled and the vapor about 10 K superheated relative to the bubble point, with a flat interface, in a closed tank. Dissolved CO_2 is carried as a one-way-coupled tracer for the freeze-out assessment and does not affect the flow or temperature fields; it plays no role here. Because CO_2 is a passive tracer, runs that differ only in CO_2 content are effectively replicates; their differences measure numerical scatter and not a CO_2 effect.

Table 2. Runs used in the benchmarking (50% fill in all runs)

Group	*p* (bar)	CO_2 (mol%)	Excitation	Runs
Sloshing	10	0.5, 1, 2, 3	0.4 Hz, 3°	4
Sloshing	15	1, 2, 3	0.4 Hz, 3°	3
Sloshing	20	1, 2, 3	0.4 Hz, 3°	3
Sloshing	25	1, 2, 3	0.4 Hz, 3°	3
Sloshing	30	2	0.4 Hz, 3°	1
Static (paired)	10; 15; 15; 25	3; 1; 2; 2	None	4

Validation in the strict sense requires simulating the experimental configuration itself. The reference tank of Ludwig et al. [2] is a vertical cylinder of 0.148 m radius holding liquid nitrogen at about 250 kPa under lateral excitation, and none of the present runs reproduces it; no validation against this reference is therefore claimed. What is performed is a non-dimensional benchmarking: the results are expressed in the dimensionless groups that the reference built to make its findings independent of geometry and fluid, and placed beside the data for three fluids. Such a comparison can reveal consistency or inconsistency, but it does not replace direct validation.

2.5. Dimensionless groups and extraction procedure

The framework replaces the molecular thermal diffusivity of the liquid, D_0, by an effective diffusivity, D_e, that lumps surface renewal and wave-induced mixing. Their ratio is the sloshing Nusselt number, which is governed by a sloshing Reynolds number built on the wave amplitude b, the angular excitation frequency ω and the liquid kinematic viscosity ν_l. The strength of phase change is measured by the Jakob number, in which Θ is the subcooling of the bulk liquid with respect to the saturation temperature at tank pressure and Δh_{lv} is the latent heat:

$$Nu_S = \frac{D_e}{D_0} \tag{2}$$

$$Re_S = \frac{\omega b^2}{\nu_l} \tag{3}$$

$$Ja = \frac{\rho_l c_{p,l} \Theta}{\rho_{v,s} \Delta h_{lv}} \tag{4}$$

The correlation of Ludwig et al. [2], which collapses the data of all three fluids over three decades of Reynolds number, reads

$$Nu_S = \left(\frac{Re_S}{Re_c}\right)^{0.69} \tag{5}$$

with a critical Reynolds number $Re_c = 4 \times 10^3$ (±20%), below which sloshing has no appreciable effect on heat transfer. The viscosity uncertainty of Section 2.3 places the present points on the Reynolds axis to within about 15%, which is small compared with the width of the experimental range.

The reduced model of the reference obtains the condensation velocity w_c from the thickness of the thermal boundary layer, δ_T, which for an interface that is sharp at $t = 0$, the initial state of all present runs, grows with the square root of

ARTICLE IN PRESS

time. Integrating over the run duration τ gives the height W of the condensed vapor column per unit free-surface length S, which is inverted to obtain D_e from the cumulative condensed mass Δm_c:

$$w_c = \frac{D_e Ja}{\delta_T}, \quad \delta_T = \sqrt{\pi D_e t} \tag{6}$$

$$W = \frac{\Delta m_c}{\rho_{v,s} S} = 2Ja\sqrt{\frac{D_e \tau}{\pi}} \quad \Rightarrow \quad D_e = \frac{\pi W^2}{4Ja^2 \tau} \tag{7}$$

Substituting the Jakob number of Eq. (4) into Eq. (7) removes the saturated-vapor density $\rho_{v,s}$:

$$D_e = \frac{\pi \, \Delta m_c^2 \Delta h_{lv}^2}{4S^2 \rho_l^2 c_{p,l}^2 \Theta^2 \tau} \tag{8}$$

D_e, Re_S, Pr and E contain no vapor density, so the extraction does not depend on the vapor-density model. The simulated condensed mass, the pressure history and, through the pressure, Θ do depend on it, because the ideal-gas vapor underestimates the inventory and heat capacity of the ullage; the bias grows from 12% at 10 bar to 30% at 30 bar (Section 2.3), and the 25 and 30 bar results are therefore regarded as qualitative. All inputs come from the recorded reports of each run: Δm_c from the time integral of the condensation rate; b, the time-averaged wave amplitude, taken as half of the crest-to-trough excursion between the maximum and minimum free-surface probe heights on the α = 0.5 iso-surface and averaged after the initial transient, which is the realized wave amplitude on which the sloshing Reynolds number of Ludwig et al. is built; S from the liquid volume and the section geometry; and Θ_w, the window mean of the subcooling, from the saturation temperature at the instantaneous pressure and the mean liquid temperature. Liquid properties are evaluated with the same property functions used in the simulations, and Ja and $\rho_{v,s}/\rho_l$ with the GERG-2008 saturated-vapor density. In two dimensions, Δm_c and S are taken per unit depth.

Eqs. (6)–(8) assume square-root growth of the thermal boundary layer from a sharp initial interface. Since neither the static nor the sloshing runs follow this law (Section 3.3), D_e is an equivalent, window-dependent value, and Nu_S and E must be read in that sense; the 60 s window is the least sensitive and is used as the reference. Θ_w (7.1–8.7 K) is smaller than the initial subcooling (about 10 K) because condensation heats the liquid and the falling pressure lowers the saturation temperature; since $D_e \propto \Theta^2$, the choice between Θ_w and the initial value changes Nu_S by up to about a factor of two at 10 bar, which is included in the ranges of Table 4. For E (Eq. 9), Ja_0 of both members of a pair is fixed at their common initial state, so that the different thermodynamic paths of the two members do not enter E.

2.6. Two metrics and their sensitivity to the closure coefficient

Ludwig et al. [2] define the sloshing Nusselt number in practice as the ratio of the condensation rate with sloshing to that without it, and ran the unexcited test E0 for this purpose. The matched static runs play the same role here, so a paired enhancement factor is evaluated besides the absolute Nusselt number:

$$E = \frac{D_{e,slosh}}{D_{e,stat}} \tag{9}$$

with Ja_0 (the Jakob number at the common initial state) of both members fixed at their common initial state. The absolute value measures the total transfer; E measures the part added by sloshing.

The two metrics differ in their sensitivity to the closure coefficient. The source term of Eq. (1) scales with the product σa_i, and both factors are effective quantities. The response of the transfer rate to this product is sublinear: in separate sensitivity runs by the authors for a near-resonant case with pure methane (Supplementary Table S2), reducing σ ten-

ARTICLE IN PRESS

fold changed the mean transfer rate by a factor of 0.14 and increasing it ten-fold by a factor of 2.0. Since D_e in Eq. (8) scales with the square of the condensed mass, a ten-fold change in σ moves the absolute Nusselt number by about four times in one direction and up to about fifty times in the other. Removing the 2.8-fold deficit of a_i would, with the same response, raise the absolute level by about a factor of two and widen, not reduce, the gap to the correlation. The absolute comparison is therefore an order-of-magnitude consistency test without discriminating power. These factors were obtained for pure methane near resonance, and their transfer to the present mixture is itself an extrapolation; they are indicative only. In the same series, replacing the realizable k–ε model by SST k–ω changed the HKS mean transfer rate by −0.7% and the normalized pressure at 35 s by 0.006 (Supplementary Table S2).

Two consequences follow. First, a kinetic coefficient can only hold the interfacial flux below the limit set by heat transport in the liquid; it cannot raise it above that limit. If heat transport in the liquid were purely molecular, the extraction would return $Nu_S \leq 1$ for any σ; the limit of large σ with pure conduction is the behavior of the unexcited test. A static Nusselt number above unity therefore shows that the effective liquid-side transport of the numerical framework exceeds molecular transport, and cannot be attributed to the choice of σ. The departure of the static condensation rate from the square-root law (Section 3.3) does not weaken this argument, because pure conduction gives exactly that law; it only means that D_e in the static case is an equivalent, window-dependent value. Second, because σa_i is common to both members of a pair, E is expected to be less sensitive to it than the absolute level. This has not been tested: the sublinear response may differ between the static state, in which condensation heat accumulates beneath the interface and throttles the source, and the sloshing state. Because this self-throttling is stronger in the static state, a smaller σ would probably reduce E and a larger one increase it; this direction is also untested and says nothing about the correct value of an effective, mesh-dependent σ. The conclusions below therefore rest mainly on E and on the mixed-layer mechanism, and the absolute comparison of Section 3.2 is reported conditionally.

2.7. Applicability of the correlation

The benchmarking is also limited by known differences between the two systems: rotational versus lateral excitation; a shallow horizontal tank versus a deep vertical cylinder; the two-dimensional domain, which captures only planar waves; vapor-to-liquid density ratios beyond the experimental range at the higher pressures; the multicomponent fluid; and the initial state, since the experiments start after a settling period with a developed boundary layer whereas the simulations start from a sharp interface.

Table A2 (Appendix A) lists the differences between the experimental reference and the present simulations together with their treatment and expected influence. Re_S is built on the realized wave amplitude, so the correlation is device-independent by construction, but the influence of rotational forcing, of the horizontal geometry, of the two-dimensional domain (planar waves only; the interface available for transfer is probably underestimated) and of the pseudo-pure fluid cannot be quantified from the present data. With the $Pr^{1/3}$ dependence reported by the reference, the Prandtl-number effect on Nu_S is up to about 8% (Section 3.1). Ja below, and the vapor-to-liquid density ratio above, the experimental range at high pressure make the 25 and 30 bar results an extrapolation.

ARTICLE IN PRESS

3. Results and discussion

3.1. Matching of dimensionless groups

Table 3 compares the dimensionless groups of the present runs with the experimental database. The sloshing Reynolds numbers fall inside the experimental range, so the comparison is an interpolation, the main condition for applying an empirical correlation. The Prandtl number of the mixture (1.98–2.23) is close to that of liquid nitrogen (about 2.5); with the one-third-power dependence of Nu_S on Pr reported by the reference, the resulting fluid effect is up to about 8% at the lower end of the range (Pr = 1.98) and about 4% at the upper end (Pr = 2.23). Two groups lie outside the experimental range: the vapor-to-liquid density ratio reaches about three times the largest experimental value at high pressure, and Ja lies below the liquid-nitrogen range. Results at 25 and 30 bar are read with this caveat. In addition, Re_S varies only between 1.82×10^5 and 2.19×10^5, because all 14 sloshing runs share the same excitation; the comparison therefore tests the location of the results relative to the correlation at one Reynolds number, not its slope. Complementary 15 bar runs of the same model at other frequencies and amplitudes (Supplementary Table S4) show a strong response to excitation intensity (a resonance peak in the pressure drop at $f/f_n = 0.99$ and a pressure drop that grows with amplitude) and an estimated Re_S range of about $0.5–3 \times 10^5$, but Nu_S was not extracted for them.

Table 3. Dimensionless groups of the present runs and of the experimental database

Group	Present work (10–30 bar)	LN_2 [2]	LH_2 [9]	HFE-7000 [10]	Status
$Re_S/10^4$	18–22	1.4–62	6.6 and 590	5.3	Interpolation
Pr	1.98–2.23	≈2.5	≈1.3	≈6	Matched
Ja	0.65–1.34	5.9–7.1	2.4	38	Below range
$\rho_{v,s}/\rho_l$	0.038–0.130	0.014	0.047	0.011	Extrapolation at high p
Relative wave amplitude	0.15–0.20 (b/R_{tank} = b/liquid depth)	0.12–0.70 (b/R)	0.6 (b/R)	0.6 (b/R)	Planar, non-breaking waves

The tank radius equals the liquid depth at 50% fill (0.75 m), so b/R_{tank} and b/liquid depth coincide; with the free-surface half-length (L/2 = 2 m) as the analogue of the radius of a vertical cylinder, the relative amplitude would be 0.056–0.075. The relative amplitude is therefore not a matched parameter; the matching quantity is Re_S, which is built on b itself. “Planar, non-breaking waves” denotes planar waves without breaking or contact of the free surface with the tank top during the analysed window, verified from the volume-fraction fields and from the spectral analysis of the interface height, whose dominant line lies at twice the excitation frequency (0.80 Hz for the 0.40 Hz baseline). This is a qualitative regime criterion and not a threshold taken from the experiments; roof impact and wave breaking occur at 6° and at resonance.

3.2. Location relative to the Nusselt–Reynolds correlation

Table 4 lists the extracted quantities by pressure level. The range at each level includes the scatter among runs, the sensitivity to the definition of the reference subcooling (window mean versus initial value) and an alternative extraction from the pressure history. The extracted values (25–66) lie a factor of 1.6–4.8 above the correlation (13.9–15.8), a multiplicative deviation rather than an order of magnitude. On a correlation spanning three decades of Re_S and more than two of Nu_S, this indicates order-of-magnitude consistency; in view of Section 2.6, it indicates nothing more.

ARTICLE IN PRESS

Table 4. Extracted dimensionless quantities by pressure level (0.4 Hz, 3°, 50% fill)

Quantity	10 bar	15 bar	20 bar	25 bar	30 bar
Runs	4	3	3	3	1
Θ (K)	7.1	8.5	8.6	8.6	8.7
Ja	1.34	1.14	0.90	0.75	0.65
$\rho_{v,s}/\rho_l$	0.038	0.058	0.079	0.102	0.130
b (m)	0.149	0.142	0.130	0.121	0.111
$Re_S/10^5$	2.19	2.14	2.08	2.00	1.82
Nu_S, present	25–36	37–51	44–60	49–66	51–66
Nu_S, Eq. (5)	15.8	15.6	15.3	14.9	13.9
Ratio*	2.3	3.3	4.0	4.5	4.8

* Evaluated from the upper bound of each range; for the paired runs, which lie near the lower bound, see Section 3.2.

The deviation is nevertheless systematic: it grows steadily with pressure while Re_S stays nearly constant. The paired runs identify its origin between 10 and 25 bar, where static references exist (the 30 bar point has none). Since the sloshing Nusselt number is the product of the static baseline and *E*, its ratio to the correlation splits into these two factors. The ratio of the static baseline to the correlation rises from 0.66 at 10 bar to 0.92 at 15 bar and 1.25 at 25 bar, whereas *E* changes only from 2.52 to 2.69; on a logarithmic scale about 91% of the trend comes from the baseline and 9% from *E*. The products of the two factors are 1.66, 2.40 and 3.36; they differ from the last row of Table 4 because that row uses the upper bound of each range, whereas the paired runs lie near the lower bound. What grows with pressure is therefore the baseline transfer of the model without sloshing, not the sloshing enhancement.

Part of this growth is a property effect. D_0, evaluated with GERG-2008 at the mean liquid temperature, falls from 11.5×10^{-8} m^2 s^{-1} at 10 bar to 9.4×10^{-8} m^2 s^{-1} at 25 bar, a factor of 1.22, whereas the static baseline grows by a factor of 1.79. About one third of the growth (on a logarithmic scale) is thus the decrease of the denominator of Nu_S; the remainder, a factor of about 1.46, is a genuine increase of the static effective diffusivity with pressure. Its cause cannot be identified from the present data. Candidates acting in the same direction are the declining share of the interfacial kinetic resistance in the Schrage flux as the saturation curve steepens, and the effect of the ideal-gas vapor on the simulated condensation itself (not on the extraction, which is independent of it). Part of the growth of the deviation with pressure may also reflect the limited applicability of the correlation at these conditions, since Ja lies below, and the density ratio above, the experimental range at high pressure (Table 3); this contribution cannot be separated here.

All runs start from a flat interface, with liquid about 10 K subcooled and vapor about 10 K superheated relative to the bubble point, in a closed tank, whereas the experiments start after a settling period with a developed thermal boundary layer. Wall heat ingress over 60 s is negligible (equivalent wall coefficient 0.036 W m^{-2} K^{-1}, fluxes of order 10 W m^{-2}), so the results are governed by this initial state and not by wall modelling. The sharp initial interface is the limiting case assumed by Eq. (6), so the extracted D_e is a start-up value and depends on the averaging window (Section 3.3). The initial vapor superheat additionally drives a rapid sensible cooling of the ullage, which accounts for 74–90% of the simulated pressure drop (Section 3.4). Earlier runs of the same model for pure methane show that the initial thermal state changes the transient condensation: reducing the initial vapor–liquid temperature difference from 23.3 K to 13.3 K lowered the pressure drop in the first half of the run and made the pressure histories of the two closures cross at about 34 s. Both members of each static–sloshing pair share the initial state, so E is expected to be less sensitive to it than Nu_S; this was not tested.

ARTICLE IN PRESS

3.3. Static reference and partition of the transfer

In the unexcited experiment of the reference, D_e equals the molecular diffusivity and $Nu_S = 1$, the zero of the scale. The same extraction applied to the four static runs gives 10.4–18.6 (Fig. 1a, Table 5): before any sloshing is applied, the static reference of the model is already about one order of magnitude more diffusive than pure conduction.

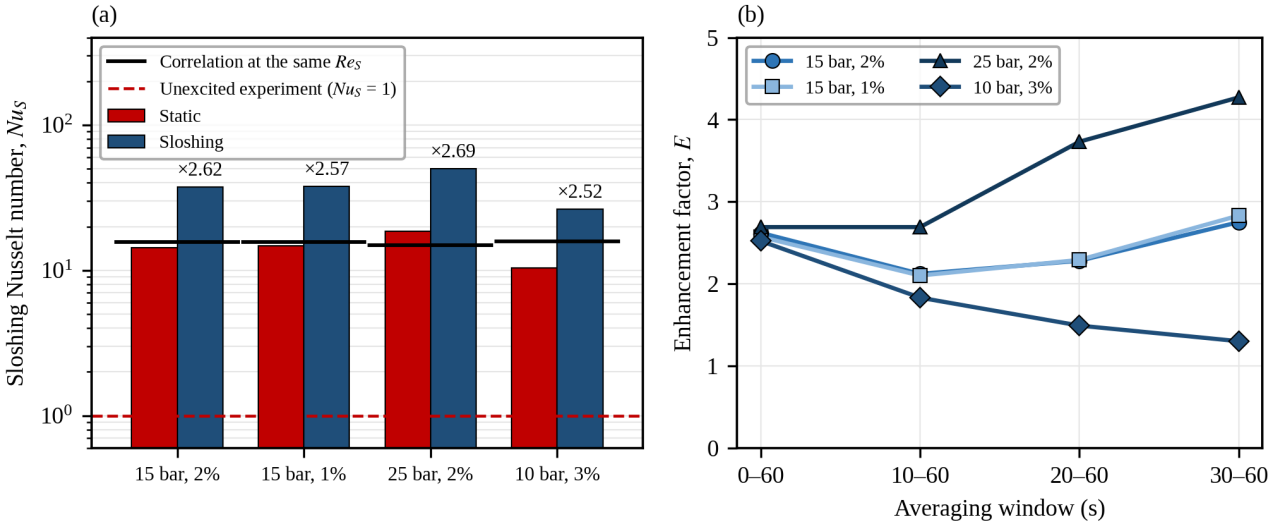


Fig. 1. (a) Partition of the sloshing Nusselt number into static baseline and sloshing enhancement for the four matched pairs; (b) sensitivity of the enhancement factor to the averaging window.

Table 5. Enhancement factor of the effective diffusivity for the matched static–sloshing pairs (60 s window)

Pair	Nu_S, sloshing	Nu_S, static	E	Correlation at same Re_S
15 bar, 2%	37.4	14.3	2.62	15.6
15 bar, 1%	37.7	14.7	2.57	15.6
25 bar, 2%	50.0	18.6	2.69	14.9
10 bar, 3%	26.3	10.4	2.52	15.8

E lies between 2.52 and 2.69 in all four pairs although pressure varies from 10 to 25 bar and CO_2 content from 1 to 3 mol%. At a single Reynolds number the enhancement therefore shows no dependence on pressure over 10–25 bar; its independence of CO_2 content follows from the treatment of CO_2 as a passive tracer. This rests on four pairs, i.e., three distinct thermodynamic states, since the two 15 bar pairs are effectively replicates (they differ by at most about 3% in Nu_S and 2% in E), and it says nothing about the slope of the correlation. The same factor is, however, about six times smaller than the correlation value at the same Reynolds number (about 15). Because the static baseline is already high, the room left for the sloshing enhancement is compressed; the product of baseline and enhancement (26–50) is the absolute value of Section 3.2 and lies within a factor of 1.7–3.4 of the experimental level. The model thus reproduces the total interfacial transfer within a multiplicative factor but does not partition it correctly between baseline and enhancement. The high baseline cannot be attributed to the closure coefficient: as shown in Section 2.6, a kinetic coefficient can only hold the flux below the liquid-side transport limit, and purely molecular transport would give $Nu_S \leq 1$. The baseline reflects the effective liquid-side transport of the numerical framework.

Fig. 1b shows that E depends on the averaging window and ranges from 1.3 to 4.3. The reason is that in neither the static nor the sloshing runs does the condensation rate decay with the square root of time: boundary-layer growth is arrested in both, whereas in the experiment only the sloshing state behaves this way. Table 5 uses the full 60 s window, which is the least sensitive and gives consistent values for all pairs; the narrowness of the 2.52–2.69 range is

ARTICLE IN PRESS

conditional on this choice. The main conclusion is not: over the whole window-dependent range, E remains 3.5–12 times smaller than the correlation value. The 91%/9% decomposition of Section 3.2 refers to this window.

The high static baseline is traced to the numerical framework rather than to the closure coefficient. In a control run identical to the 15 bar static baseline but without a turbulence model (not a member of the matched pairs; time step 0.005 s; record starting at 5.25 s), the ullage pressure fell by only 0.11% up to 60 s and the vapor temperature remained unchanged, whereas the static run with the realizable k–ε model reached a pressure drop of 3.84% and a vapor cooling of 4.3 K at 60 s (Supplementary Table S2). In the k–ε fields the ratio of eddy to molecular viscosity reaches about 10^4, although the resolved velocity in the static runs is only about 0.04 m s^{-1}. The realizable k–ε model without a buoyancy-damping term therefore produces non-physical eddy diffusion in the stably stratified quiescent layer, which is the main source of the excess static transport. Under-resolution is a second contribution: the conduction boundary layer grows from about 1.3 mm at 1 s to 4.1 mm at 10 s and 10.2 mm at 60 s, so with 3.2 mm cells in the interfacial band it is resolved by fewer than two cells during the first 10 s; numerical diffusion of the VOF interface, which averages temperature over two-phase cells, adds to this. The relative shares of the three effects were not separated, and Nu_S was not extracted from the laminar run because of its different time step and truncated record. For the wave-dominated sloshing case, replacing the realizable k–ε model by SST k–ω changed the HKS results by less than 1%, but this test does not probe a stratified static layer.

3.4. Pressure history versus the reduced model

The reduced model of the reference was integrated forward with the correlation Nusselt number and the thermodynamic state of each run, and also with the molecular diffusivity (Fig. 2). The final pressure drop is reproduced to within about one percentage point at all five pressures. However, 74–90% of the pressure drop comes from sensible cooling of the vapor and only the remainder from condensation; since the reduced model, like the original relation of the reference, takes the vapor temperature from data, much of this agreement is self-referential. The meaningful comparison is that of the condensation component: its simulated-to-model ratio is 1.12, 1.19 and 1.08 at 10, 15 and 20 bar, within 20%, and falls to 0.83 and 0.42 at 25 and 30 bar.

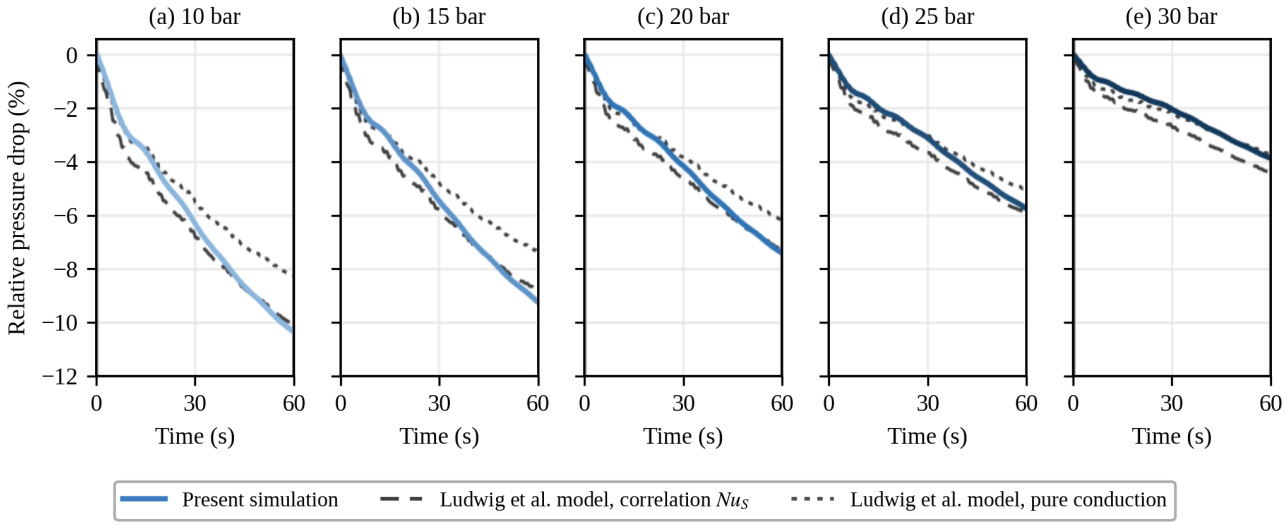


Fig. 2. Relative pressure drop at the five pressure levels: simulation versus the reduced model of Ludwig et al. [2] with the correlation Nusselt number and with pure conduction.

ACCEPTED IN PRESS

Two candidates, both growing with pressure and not separable with the present data, explain this divergence. The first is thermal expansion of the liquid, neglected by the reduced model and negligible in the experiment: condensation heat raises the bulk liquid temperature by about 1.3 K and its volume by about 0.6%, which compresses the ullage and offsets part of the condensation-driven pressure drop. The second is the ideal-gas vapor (Table 1), which at 25 and 30 bar ($Z = 0.69$ and 0.65) underestimates vapor density by about 25% and 30% and hence the inventory and heat capacity of the ullage. The mass-based comparison of Section 3.2 is therefore the cleaner metric. The 25 and 30 bar results should therefore be regarded as qualitative.

3.5. Mixed-layer mechanism

The key finding of the experimental reference is a mechanism: under sloshing, growth of the thermal boundary layer beneath the free surface is arrested at a thickness of the order of the wave amplitude and a mixed layer forms, so the condensation rate stays nearly constant instead of decaying with the square root of time [2]. Fig. 3 shows that the simulations are qualitatively consistent with this behavior, for one case only (15 bar, 2 mol% CO_2). In the sloshing run the condensation velocity decays far more slowly than the square-root law, falling by roughly 30% over the run, whereas a $t^{-1/2}$ decay would reduce it by a factor of about 2.5–3.5 over comparable windows; in the static run it first rises for about 20 s and then decays but remains above the conduction curve, which reflects the high diffusive baseline of Section 3.3. The contrast between the two states resembles the mechanism measured experimentally and does not depend on any absolute quantity.

As supporting evidence from the same runs, the ratio of the mean interfacial CO_2 supersaturation to its bulk mean, a quantity governed by the near-interface temperature field, falls to about 0.72–0.73 at 60 s in the static tanks (15 and 25 bar), whereas under sloshing it is 0.89–0.92; in the static run without turbulence model it falls further, to 0.48. This indicates that the cold surface layer is continuously renewed under sloshing, whereas a thermal barrier forms under the interface in the static runs. Near-interface temperature profiles were not stored and are not shown, and the agreement rests on one case and is therefore described as qualitative.

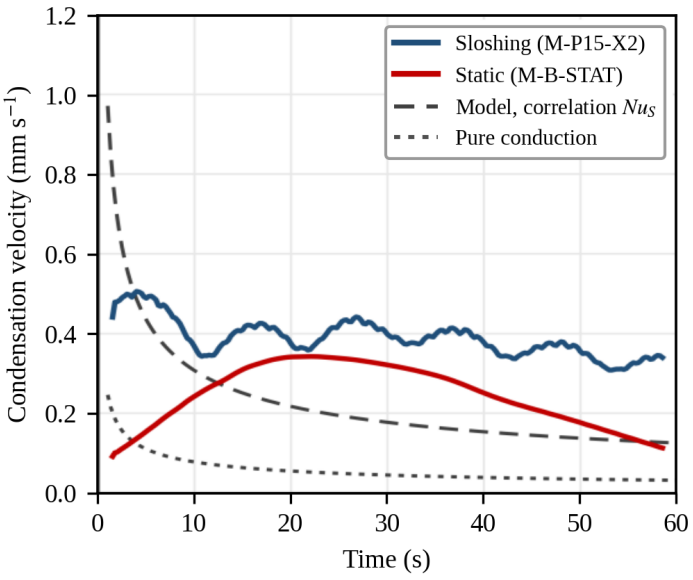


Fig. 3. Condensation velocity in the matched sloshing and static runs (15 bar, 2 mol% CO_2) compared with the transient boundary-layer model with the correlation Nusselt number and with pure conduction.

ARTICLE IN PRESS

3.6. Implications for process design

(i) Screening of CFD models. A single pressure curve can be matched by compensating errors. Reporting Nu_S and the static-to-sloshing partition against the correlation gives a simple acceptance check before a VOF–phase-change model is used to size pressure-management measures. The present model passes an order-of-magnitude test (factor 1.6–4.8 at one Reynolds number) but not the partition test, so absolute condensation rates predicted without calibration should be treated as order-of-magnitude values and carry a corresponding uncertainty in design.

(ii) Pressure management and condensation prediction. In the matched pairs, sloshing amplifies the 60 s pressure drop by a factor of 2.24–2.49 and the vapor cooling by 2.24–2.92 relative to the static runs, and 74–90% of the simulated drop is sensible cooling of the superheated vapor. Depressurization predictions must therefore include the ullage energy balance and not condensation alone, and the initial thermal state of the ullage matters as much as the sloshing intensity for short-term depressurization. Once the realized wave amplitude is known, the reduced model (Eqs. 5–8) gives a rapid estimate of the condensation component.

(iii) Safety margins. At 25 and 30 bar the vapor-to-liquid density ratio exceeds the experimental range by up to a factor of about three and the ideal-gas vapor density is 25–30% low, so predictions there are qualitative and should be covered by margins. Because the net bias under sloshing is not determined (the model overestimates static transport and underestimates the sloshing enhancement), a simulated pressure collapse should not be assumed conservative; bounding cases for both effects should be considered.

(iv) Scope. The runs are short (60 s), two-dimensional and, for practical purposes, adiabatic; long-term heating over a voyage is not represented, and the benchmark does not validate CO_2 freeze-out (Section 3.7).

3.7. Freeze-out risk assessment: qualitative outlook

The benchmarking provides no support for the freeze-out risk layer applied to these runs, because the reference fluid is single-component and offers no data on dissolution or solid formation; that layer rests on its own solid–liquid equilibrium and nucleation-kinetics calibration, and no supersaturation results are shown here. Qualitatively, excess mixing keeps the surface layer colder than in reality and overestimates the interfacial supersaturation, which is conservative for interface-based measures; it also removes the initial bulk subcooling faster and slightly underestimates the peak bulk supersaturation, which is non-conservative for bulk measures. Because the model overestimates the static transport but underestimates the sloshing enhancement, the net bias under sloshing is not obvious.

4. Conclusion

Sloshing simulations of a PLNG mixture in a Type-C tank were benchmarked against the sloshing Nusselt–Reynolds correlation of Ludwig et al. The benchmarking supports three points:

- **Scaling.** The paired enhancement factor (2.52–2.69 over a 60 s window), a ratio expected to be less sensitive than the absolute level to the closure coefficient, shows no dependence on pressure over 10–25 bar at a single Reynolds number (three distinct thermodynamic states); independence of CO_2 content follows from its treatment as a passive tracer, and E varies from 1.3 to 4.3 for other averaging windows. The slope of the correlation is not tested.

ARTICLE IN PRESS

- **Mechanism.** The arrest of thermal boundary-layer growth under a mixed layer, the central finding of the experiments, is reproduced qualitatively for one case (15 bar, 2 mol% CO_2).
- **Magnitude.** The sloshing Reynolds numbers lie inside the experimental range and the extracted Nusselt numbers lie within a factor of 1.6–4.8 of the correlation; since the absolute level depends on the closure coefficient, this is order-of-magnitude consistency only.

A quantified limitation was also found: the static reference of the framework is about one order of magnitude more diffusive than pure conduction, so the model reproduces the total interfacial transfer but not its partition between baseline and sloshing enhancement. This excess cannot be attributed to the closure coefficient, because a kinetic coefficient can only hold the flux below the liquid-side transport limit; a control run without turbulence model indicates that it comes mainly from eddy diffusion of the k–ε model in the stratified static layer, with under-resolution of the thermal boundary layer and numerical diffusion as further contributions. E remains 3.5–12 times below the experimental value for every averaging window, and about 91% of the growth of the deviation with pressure comes from the static baseline. Agreement of the pressure history with the reduced model is largely self-referential, and the mass-based comparison is the cleaner test. Further limitations are the single excitation (the slope of the correlation is not tested), the two-dimensional domain, the closure coefficient and the turbulence model, the sharp initial interface and the ideal-gas vapor, which makes the 25 and 30 bar results qualitative. Future work should test the sensitivity of E to σ with a matched pair, use a buoyancy-corrected or low-Reynolds turbulence model with a refined interfacial mesh, extend the benchmarking along the frequency and amplitude axes, and replace the ideal-gas vapor by a real-gas density.

Supplementary material

Supplementary material (existing results only): Table S1, per-run values of Δm_c, b, Θ, Nu_S and the correlation value for all 18 runs; Table S2, sensitivity and diagnostic runs (σ ÷ 10 and σ × 10, SST k–ω, laminar static control); Table S3, mesh studies and grid-convergence index; Table S4, complementary frequency and amplitude runs at 15 bar; Fig. S1, validation against Grotle and Æsøy [3] at three excitation frequencies.

ARTICLE IN PRESS

Appendix A. Solver settings and applicability of the correlation

Table A1. Solver settings of the production runs

Item	Setting
Software and solver	ANSYS Fluent 2023 R2; pressure-based, transient, two-dimensional planar; phase change implemented in a C user-defined function
Interface	VOF with geometric reconstruction (PLIC); no additional interface-compression term
Pressure–velocity coupling; pressure	PISO; PRESTO!
Spatial discretization	Second-order upwind for momentum, energy, density, k and ε
Time stepping	Second-order implicit; $\Delta t = 0.0005$ s; Courant number about 1–2 at the maximum velocity and below 1 for most of the run; 60 s per run; reports every 0.25 s
Convergence	Residuals 10^{-4} (continuity, momentum) and 10^{-6} (energy); at most 60 iterations per time step
Under-relaxation	0.3 (pressure); 0.7 (momentum, k, ε, body force); 0.9 (density, energy)
Turbulence	Realizable k–ε with standard wall functions, no buoyancy-damping term; also in the static runs
Motion	Rigid-body rotation of the mesh (dynamic mesh, geometric conservation law); $\theta = \theta_A \sin(2\pi ft)$; centre of rotation at the geometric centre of the tank bottom
Wall thermal condition	Equivalent overall heat-transfer coefficient 0.036 W m^{-2} K^{-1} to a 305 K ambient (not a conjugate calculation); heat ingress of order 10 W m^{-2}, negligible over 60 s
Initial condition; boundary	Flat interface; liquid about 10 K subcooled and vapor about 10 K superheated relative to the bubble point; closed tank without venting
Properties	Liquid properties from GERG-2008 (CoolProp) as temperature polynomials; vapor density from the ideal-gas law with the effective molar mass

Table A2. Differences between the experimental reference of Ludwig et al. [2] and the present simulations

Aspect	Ludwig et al. [2]	Present work	Treatment and expected influence
Excitation	Lateral translation of a vertical cylinder	Harmonic roll about the geometric centre of the tank bottom	Res is built on the realized wave amplitude, so the correlation is device-independent by construction; any residual effect of rotational forcing is unknown.
Geometry	Vertical cylinder, R = 0.148 m, deep liquid	Horizontal Type-C tank, 4 m × 1.5 m, 50% fill (depth 0.75 m)	Shallow-liquid planar waves in a long tank; influence unknown.
Dimensionality	Three-dimensional waves, including swirl and breaking	Two-dimensional; planar waves only	Rotational waves and three-dimensional breaking are not reproduced and the interface available for transfer is probably underestimated; the effect on Nus cannot be quantified.
Fluid	LN_2, LH_2, HFE-7000 (single component)	$CH_4/C_2H_6/C_3H_8/N_2$ = 90/6/3/1 mol%, pseudo-pure; Pr = 1.98–2.23	Pr effect up to about 8% (about 4% at Pr = 2.23); multicomponent effects such as preferential evaporation are not modelled.
Operating conditions	About 250 kPa; $\rho_{v,s}/\rho_l$ = 0.011–0.047; Ja = 2.4–38	10–30 bar; $\rho_{v,s}/\rho_l$ = 0.038–0.130; Ja = 0.65–1.34	Ja below, and density ratio above, the experimental range at higher pressures: extrapolation; 25 and 30 bar read as qualitative.
Initial state	Settling period, developed thermal boundary layer	Flat sharp interface; liquid about 10 K subcooled, vapor about 10 K superheated	Start-up transient; see Section 3.2.
Relative amplitude	b/R = 0.12–0.70 (LN_2)	b/R_{tank} = 0.15–0.20; b/(L/2) = 0.056–0.075	See Section 3.1.

Acknowledgements

This article is extracted from the Ph.D. thesis of the first author at the Department of Chemical Engineering, University of Sistan and Baluchestan, Zahedan, Iran.

Nomenclature

Symbols

a_i	Interfacial area density (m^{-1})
b	Wave amplitude (m)
c_p	Specific heat capacity (J kg^{-1} K^{-1})
D_0	Molecular thermal diffusivity of the liquid (m^2 s^{-1})
D_e	Effective diffusivity (m^2 s^{-1})

Abbreviations

CFD	Computational fluid dynamics
GERG	GERG-2008 equation of state
HKS	Hertz–Knudsen–Schrage
LNG	Liquefied natural gas
PLNG	Pressurized liquefied natural gas

ARTICLE IN PRESS

E	Paired enhancement factor (–)	VOF	Volume of fluid
f	Excitation frequency (Hz)		
Ja	Jakob number (–)		
M	Molar mass (kg mol^{-1})		
Nu_S	Sloshing Nusselt number (–)		
p	Pressure (Pa)		
Pr	Prandtl number (–)		
R	Universal gas constant (J mol^{-1} K^{-1})		
Re_S, Re_c	Sloshing and critical Reynolds numbers (–)		
S	Free-surface length per unit depth (m)		
T	Temperature (K)		
t	Time (s)		
W	Height of condensed vapor column (m)		
w_c	Condensation velocity (m s^{-1})		
Z	Compressibility factor (–)		
α	Volume fraction (–)		
δ_T	Thermal boundary-layer thickness (m)		
Δh_{lv}	Latent heat of vaporization (J kg^{-1})		
Δm_c	Cumulative condensed mass per unit depth (kg m^{-1})		
Θ	Bulk-liquid subcooling (K)		
θ_A	Roll amplitude (°)		
ν	Kinematic viscosity (m^2 s^{-1})		
ρ	Density (kg m^{-3})		
σ	Accommodation coefficient (–)		
τ	Run or averaging duration (s)		
ω	Angular excitation frequency (rad s^{-1})		
E_0	Unexcited reference experiment of Ludwig et al. (Nu_S = 1)		
Ja_0	Jakob number at the common initial state of a pair (–)		
L_{cell}	Characteristic cell length, $V_{cell}^{1/3}$ (m)		
Θ_w	Window-mean bulk-liquid subcooling (K)		

Subscripts: l, liquid; v, vapor; s, saturation; slosh, sloshing run; stat, static run

References

[1] Arndt, T., Dreyer, M., 2009. Cryogenic sloshing tests in a pressurized cylindrical reservoir, Proceedings of the 45th AIAA/ASME/SAE/ASEE Joint Propulsion Conference & Exhibit, Denver, CO, USA, AIAA Paper 2009-4860. https://doi.org/10.2514/6.2009-4860

[2] Ludwig, C., Dreyer, M.E., Hopfinger, E.J., 2013. Pressure variations in a cryogenic liquid storage tank subjected to periodic excitations, International Journal of Heat and Mass Transfer, 66, 223-234. https://doi.org/10.1016/j.ijheatmasstransfer.2013.06.072

[3] Grotle, E.L., Æsøy, V., 2018. Dynamic modelling of the thermal response enhanced by sloshing in marine LNG fuel tanks, Applied Thermal Engineering, 135, 512-520. https://doi.org/10.1016/j.applthermaleng.2018.02.086

[4] Balouchi, Y., Zivdar, M., Rahimi, R., Mohebbi-Kalhori, D., 2026. Sloshing-induced thermodynamic phenomena in cryogenic fuel tanks: A comprehensive review, Cryogenics, 157, 104316. https://doi.org/10.1016/j.cryogenics.2026.104316

[5] Hirt, C.W., Nichols, B.D., 1981. Volume of fluid (VOF) method for the dynamics of free boundaries, Journal of Computational Physics, 39 (1), 201-225. https://doi.org/10.1016/0021-9991(81)90145-5

[6] Lee, W.H., 1980. A pressure iteration scheme for two-phase flow modeling, In: Veziroglu, T.N. (Ed.), Multiphase Transport: Fundamentals, Reactor Safety, Applications, Hemisphere Publishing, Washington, DC, 407-431.

[7] Schrage, R.W., 1953. A Theoretical Study of Interphase Mass Transfer, Columbia University Press, New York. https://doi.org/10.7312/schr90162

[8] Wu, S., Ju, Y., 2023. Numerical study on pressure drops and thermal response of cryogenic fuel storage tanks under sinusoidal sloshing excitation, International Journal of Hydrogen Energy, 48 (95), 36523-36540. https://doi.org/10.1016/j.ijhydene.2023.05.270

[9] Moran, M.E., McNelis, N.B., Kudlac, M.T., Haberbusch, M.S., Satornino, G.A., 1994. Experimental results of hydrogen slosh in a 62 cubic foot (1750 liter) tank, Proceedings of the 30th AIAA/ASME/SAE/ASEE Joint Propulsion Conference, Indianapolis, IN, USA, AIAA Paper 94-3259 (NASA TM-106625). https://doi.org/10.2514/6.1994-3259

ARTICLE IN PRESS

[10] Das, S.P., Hopfinger, E.J., 2009. Mass transfer enhancement by gravity waves at a liquid–vapour interface, International Journal of Heat and Mass Transfer, 52 (5-6), 1400-1411. https://doi.org/10.1016/j.ijheatmasstransfer.2008.08.016
[11] Shih, T.-H., Liou, W.W., Shabbir, A., Yang, Z., Zhu, J., 1995. A new k-ε eddy viscosity model for high Reynolds number turbulent flows, Computers & Fluids, 24 (3), 227-238. https://doi.org/10.1016/0045-7930(94)00032-T
[12] Kunz, O., Wagner, W., 2012. The GERG-2008 wide-range equation of state for natural gases and other mixtures: An expansion of GERG-2004, Journal of Chemical & Engineering Data, 57 (11), 3032-3091. https://doi.org/10.1021/je300655b
[13] Bell, I.H., Wronski, J., Quoilin, S., Lemort, V., 2014. Pure and pseudo-pure fluid thermophysical property evaluation and the open-source thermophysical property library CoolProp, Industrial & Engineering Chemistry Research, 53 (6), 2498-2508. https://doi.org/10.1021/ie4033999
[14] Grotle, E.L., Æsøy, V., 2017. Numerical simulations of sloshing and the thermodynamic response due to mixing. Energies, 10 (9), 1338.
[15] Wu, S., Ju, Y., 2021. Numerical study of the boil-off gas (BOG) generation characteristics in a Type C LNG tank under sloshing excitation. Energy, 223, 120001.
[16] Liu, Z., Yuan, Y., Xu, B., Guo, Y., Li, C., 2021. Numerical study on thermodynamic performance in a cryogenic fuel storage tank under external sloshing excitation. International Journal of Aeronautical and Space Sciences, 22, 857–868.
[17] Liu, Z., Li, C., 2018. Influence of slosh baffles on thermodynamic performance in liquid hydrogen tank. Journal of Hazardous Materials, 346, 253–262.
[18] Duan, Z., Zhu, Y., Wang, C., Yuan, Y., Xue, H., Tang, W., 2023. Numerical and theoretical prediction of the thermodynamic response in marine LNG fuel tanks under sloshing conditions. Energy, 270, 126935.
[19] Jeon, G.M., Park, J.C., Choi, S., 2021. Multiphase-thermal simulation on BOG/BOR estimation due to phase change in cryogenic liquid storage tanks. Applied Thermal Engineering, 184, 116264.
[20] Jeon, G.M., Jeong, S.M., Park, J.C., 2024. Experimental and numerical investigation of the influences of sloshing motion on the change in boil-off gas/boil-off rate in a cryogenic liquid tank. Ocean Engineering, 298, 117173.
[21] Zhao, H., Wu, G., Chen, J., Pu, X., Wang, S., Yuan, Y., et al., 2025. Impact of fluid sloshing on BOG generation in Type B LNG tanks during ship emergency stops. Journal of Marine Science and Engineering, 13 (11), 2100.
[22] Sun, M., Zhao, Z., Gong, J., 2025. Numerical investigations on boil-off gas generation characteristics of LCO2 in Type C storage tanks under different sloshing conditions. Applied Sciences, 15 (10), 5788.
[23] Agui, J.H., Moder, J.P., 2015. Modeling of non-isothermal cryogenic fluid sloshing. AIAA Paper 2015-4072, 51st AIAA/SAE/ASEE Joint Propulsion Conference, Orlando, FL.

ARTICLE IN PRESS